

# Quantification of propidium iodide delivery with millisecond electric pulses: A model study

Miao Yu<sup>a</sup>, Hao Lin<sup>a,\*</sup>

<sup>a</sup>*Mechanical and Aerospace Engineering, Rutgers, The State University of New Jersey,  
98 Brett Road, Piscataway, NJ 08854, USA*

---

## Abstract

A model study of propidium iodide delivery with millisecond electric pulses is presented; this work is a companion of the experimental efforts by Sadik et al. [1]. Both membrane permeabilization and delivery are examined with respect to six extra-cellular conductivities. The transmembrane potential of the permeabilized regions exhibits a consistent value, which corresponds to a bifurcation point in the pore-radius-potential relation. Both the pore area density and membrane conductance increase with an increasing extra-cellular conductivity. On the other hand, the inverse correlation between propidium iodide delivery and extra-cellular conductivity as observed in the experiments is quantitatively captured by the model. This agreement confirms that this behavior is primarily mediated by electrophoretic transport during the pulse. The results suggest that electrophoresis is important even for the delivery of small molecules such as propidium iodide. The direct comparison between model prediction and experimental data presented in this work helps validate the former as a robust predictive tool for the study of electroporation.

**Keywords:** Electroporation, Electrophoresis, Diffusion, Electrical conductivity, Field-amplified sample stacking

---



---

\*Corresponding Author. Tel.: +1 848 445 2322; fax: +1 732 445 3124.  
Email address: hlin@jove.rutgers.edu (Hao Lin)

## 1. Introduction

Electroporation is a widely-used technique to deliver active agents into biological cells and tissue [2, 3, 4, 5, 6, 7, 8, 9, 10]. The process includes two basic aspects. In the first, the application of an electric pulse permeabilizes the membrane to gain access to the cytoplasm [11, 12, 13, 14, 15, 16, 17, 18, 19, 20, 21, 22, 23, 24]. In the second, molecules are transported into the cell via mechanisms such as electrophoresis, diffusion, and endocytosis [5, 25, 26, 27, 28, 29, 30, 31, 32, 33, 34, 35, 36, 37, 38, 39, 40, 41, 42, 43]. In an earlier work by one of us (HL [1], henceforth denoted as Sadik13), we used time- and space-resolved fluorescence microscopy to quantify the second aspect, namely, the transport of small molecules via electroporation. This study aimed to differentiate contributions to total delivery by the various pertinent mechanisms. In addition, it also provided quantitative data to help interpret trends observed in earlier experiments, namely, the inverse correlation between delivery and extra-cellular conductivity [14, 44]. The current work complements the experimental efforts of Sadik13 with a model study.

The model couples the asymptotic Smoluchowski equation (ASE) [20, 45, 46] for membrane permeabilization with the Nernst-Planck equations for ionic transport [47, 48]. (A list of abbreviations is given in Table 1.) Following Sadik13, the delivery of propidium iodide (PI) into 3T3 mouse fibroblast cells is simulated. The extra-cellular conductivity is varied between 100 and 2000  $\mu\text{S}/\text{cm}$ . The simulation provides detailed, dynamic predictions that were not directly measured by the experiments, including the systematic behavior of the transmembrane potential (TMP), the membrane conductance, and the pore area density (PAD). On the other hand, the results on PI delivery is compared directly with data from Sadik13. This comparison not only validates the numerical model, but also helps tackle the basic physical processes involved in electroporation-mediated molecular delivery.

## 2. Model formulation

A schematic of the problem is presented in Fig. 1. A constant pulse with the strength of  $E_0$  is applied, and axisymmetry is assumed with respect to the direction of the electric field. A spherical coordinate system  $(r, \theta)$  is adopted, and the cell radius is  $a$ . The axis of symmetry is denoted by  $x$ , which is also the coordinate along the cell centerline. The intra- and extra-cellular

Abbreviation	Definition
ASE	asymptotic Smoluchowski equation
FASS	Field-Amplified Sample Stacking
PAD	pore area density
PI	propidium iodide
Sadik13	reference [1]
TFI	total fluorescence intensity
TMP	transmembrane potential

Table 1: Definition of abbreviations.

conductivities are denoted by  $\sigma_i$  and  $\sigma_e$ , respectively. The PI molecule is a charged ion with a valence number of +2.

The model framework follows that presented in earlier work [46, 47, 48]. Specifically, the permeabilization model (including the electrical problem) follows Krassowska and Filev [46]; the transport model was developed by the current authors [47, 48]. A brief summary is presented below. For reference, detailed definitions of pertinent variables are given in Appendix A.

Briefly speaking, the Ohmic equations are solved for the intra-cellular electric potential,  $\Phi_i$ , and the extra-cellular electric potential,  $\Phi_e$ :

$$\nabla \cdot (\sigma_{i,e} \nabla \Phi_{i,e}) = 0. \quad (1)$$

On the membrane, the current density continuity condition is applied:

$$-\mathbf{n} \cdot \sigma_i \nabla \Phi_i = -\mathbf{n} \cdot \sigma_e \nabla \Phi_e = C_m \frac{\partial V_m}{\partial t} + j_p, \quad (2)$$

where  $\mathbf{n}$  is the local unit vector normal to the membrane,  $C_m$  is the membrane capacitance, and  $j_p$  is the local ionic current density across electropores. The TMP (denoted by  $V_m$ ) is the potential difference across the infinitesimally-thin membrane. Equations (1, 2) are coupled with the ASE for membrane permeabilization to track the evolution of both the electric potential and pore statistics.

$$\frac{dN}{dt} = \alpha e^{(V_m/V_{ep})^2} \left( 1 - \frac{N}{N_0 e^{q(V_m/V_{ep})^2}} \right), \quad (3)$$

$$\frac{dr_j}{dt} = U(r_j, V_m, \tau). \quad (4)$$

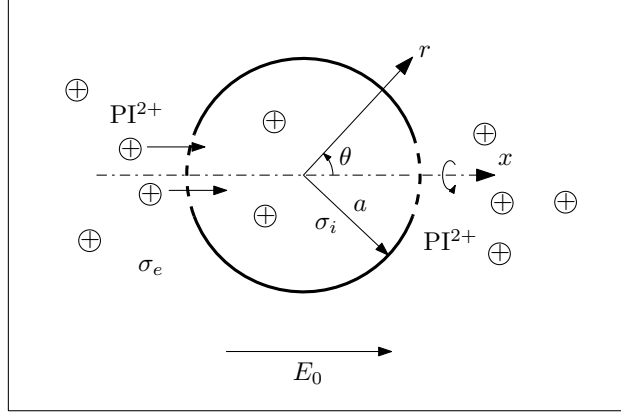


Figure 1: A schematic of the problem.  $(r, \theta)$  denotes the spherical coordinate system.  $x$  is the axis of rotation, and is aligned with the direction of field application. The field strength is denoted by  $E_0$ . The intra- and extra-cellular conductivities are denoted by  $\sigma_i$  and  $\sigma_e$ , respectively.

Here  $N(t, \theta)$  is the local pore number density.  $\alpha$ ,  $N_0$ ,  $q$  and  $V_{ep}$  are constants.  $U$  is the advection velocity, and  $\tau$  is an effective membrane tension. According to Krassowska and Filev [46], pores nucleate at an initial radius,  $r_* = 0.51$  nm, and at a rate described by Eq. (3). They then evolve in size according to Eq. (4), where  $r_j$  is the pore radius. Once Eqs. (3, 4) are solved, the current density through the pores,  $j_p$ , can be calculated, and used in Eq. (2) (see Eqs. (14, 15) in Appendix A). Based on the pore statistics according to Eqs. (3, 4), we can also compute the PAD,  $\rho_p$ :

$$\rho_p(t, \theta) = A_p(t, \theta) / \Delta A, \quad (5)$$

where  $\Delta A$  is a local area element [46], and  $A_p$  is the total area occupied by the pores thereon (see Eq. (16) in Appendix A). The PAD therefore represents a quantification of the degree of membrane permeabilization. The effective membrane conductance,  $g_m$ , is calculated by taking the ratio of the local ionic current density and the TMP:

$$g_m(t, \theta) = j_p / V_m. \quad (6)$$

Three molecular species are considered in this study, which follow the reactive kinetics



Symbol	Definition	Value/Source
$E_0$	applied field strength	0.8 kV/cm [1]
$t_p$	pulse length	100 ms [1]
$a$	cell radius	7 $\mu\text{m}$ [1]
$\sigma_e$	extra-cellular conductivity	100-2000 $\mu\text{S}/\text{cm}$ [1]
$\sigma_i$	intra-cellular conductivity	4000 $\mu\text{S}/\text{cm}$ [48]
$[\text{PI}^{2+}]_{e,o}$	initial extra-cellular concentration of $\text{PI}^{2+}$	100 $\mu\text{M}$ [1]
$[\text{B}]_{i,o}$	initial intra-cellular concentration of B	6.93 mM [48]
$V_{ep}$	characteristic electroporation voltage	0.16 V [49]

Table 2: List of model parameters.

Here  $\text{PI}^{2+}$  denotes the free PI ion, B denotes the binding sites in the cytoplasm, and PIB is the compound which is responsible for the experimentally observed fluorescence emission.  $k_+$  and  $k_-$  are the association and dissociation constants, respectively. The species concentrations are denoted by  $[\text{PI}^{2+}]$ ,  $[\text{B}]$ , and  $[\text{PIB}]$ , respectively, and obey the Nernst-Planck equations for ionic transport:

$$\frac{\partial X}{\partial t} = \nabla \cdot (\omega F z X \nabla \Phi) + \nabla \cdot (D \nabla X) + \dot{R}. \quad (8)$$

Here  $X$  is  $[\text{PI}^{2+}]$ ,  $[\text{B}]$ , or  $[\text{PIB}]$ ,  $F$  is Faraday constant.  $\omega$ ,  $z$ , and  $D$  are the electrophoretic mobility, valence number and molecular diffusivity of the species considered, respectively.  $\dot{R}$  is a source term due to chemical production according to (7). Equation (8) is solved for each species both within and outside the cell, subject to a flux condition on the membrane. A complete description of the model, including the numerical implementation, as well as the boundary and initial conditions, are found in [47, 48], and are not presented here for brevity. Model parameters specific to the current problem are listed in Table 2, which follows the experimental conditions in Sadik13. Note that in particular we adopted a value of 0.16 V for  $V_{ep}$ , the characteristic voltage of electroporation. The value differs from that used in previous work [46, 47, 48], and is determined from a comparison between experimental data and model simulation in our recent study [49].

### 3. Results

In the following, we first present simulated results on the effect of extra-cellular conductivity on membrane permeabilization. The results on PI deliv-

ery are then presented and compared with experimental data from Sadik13. For all cases, a single pulse of 0.8 kV/cm and 100 ms is applied.

Figure 2 summarizes the results on the TMP,  $V_m$ , the effective membrane conductance,  $g_m$ , and the PAD,  $\rho_p$ . Figure 2a shows the evolution of  $V_m$  at  $\theta = \pi$  as a function of time. The differences between the cases are only visible in the initial stage ( $\sim 10 \mu\text{s}$ , see the inset), which is caused by the dependence of charging time on the extra-cellular conductivity [50, 51]. For  $t > 10 \mu\text{s}$ ,  $V_m$  settles to an equilibrium value, which is maintained until the end of the pulse. Figure 2b shows  $V_m$  as a function of the polar angle,  $\theta$ , at  $t = 95 \text{ ms}$ . The consistency of the equilibrium distribution with respect to the extra-cellular conductivity is evident. We find that this equilibrium value of  $V_m$  in the permeabilized regions is determined by a critical point of the pitchfork bifurcation in the  $(r_{eq}, V_m)$  space, where  $r_{eq}$  is the equilibrium pore size at a given voltage. In other words, it is determined by the energy landscape of the porated membrane, which does not change with respect to the extra-cellular conductivity. A more detailed analysis is presented in Appendix B for interested readers.

Figure 2c shows the evolution of  $g_m$  as a function of time. Similar to  $V_m$ , it exhibits an initial stage of rapid growth, followed by a plateau (an equilibrium) in the presence of the pulse, and a rapid decay post-pulsation. However, the equilibrium value depends strongly and positively on  $\sigma_e$ . This trend is more obviously observed in Fig. 2d, where  $g_m$  at  $\theta = 0, \pi$  and  $t = 95 \text{ ms}$  is plotted against  $\sigma_e$ . This correlation is derived from the global Ohmic current balance. In fact, following an analysis similar to that presented in [48], we can show

$$g_m \propto \frac{\sigma_e}{2\sigma_e + \sigma_i} \left( 3 - \frac{2}{E_0 a} \max(|V_m|) \right). \quad (9)$$

The details are not presented here for brevity. In Fig. 2d, the dashed line represents a fitting in the form  $C\sigma_e/(2\sigma_e + \sigma_i)$ , where the fitting constant  $C = 1.46 \times 10^5 \text{ S/m}^2$ . This result is in qualitative agreement with the numerical study by Suzuki et al. [52].

Figures 2e and f show the behavior of  $\rho_p$  with respect to time and  $\sigma_e$ . Not surprisingly, the trend concurs with that of  $g_m$ , as the change in the latter is only caused by a change in membrane permeabilization. Note that this result qualitatively defers from that in supra-electroporation, where our model did not indicate a strong dependence of  $\rho_p$  on  $\sigma_e$  [48]. However, in neither situation does membrane permeabilization provide a viable explanation

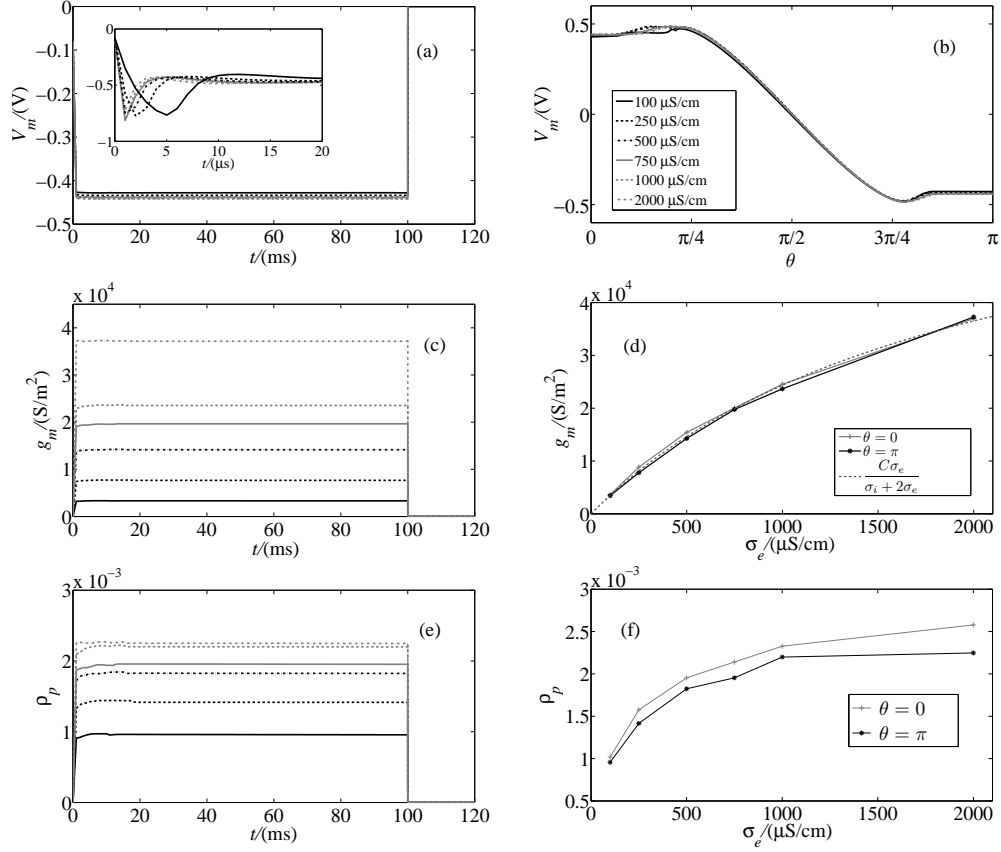


Figure 2: Simulated membrane permeabilization under a single pulse of 0.8 kV/cm in strength and 100 ms in length, for various extra-cellular conductivities. (a) Evolution of the TMP,  $V_m$ , at  $\theta = \pi$  as a function of time. (b) Polar distribution of the TMP at  $t = 95$  ms. (c) Evolution of local membrane conductance,  $g_m$ , at  $\theta = \pi$  as a function of time. (d) Membrane conductance at  $\theta = 0, \pi$  at  $t = 95$  ms. The dashed is a theoretical prediction, and the fitting constant  $C = 1.46 \times 10^5 \text{ S}/\text{m}^2$ . (e) Evolution of the PAD,  $\rho_p$ , at  $\theta = \pi$  as a function of time. (f) The PAD at  $\theta = 0, \pi$  at  $t = 95$  ms.

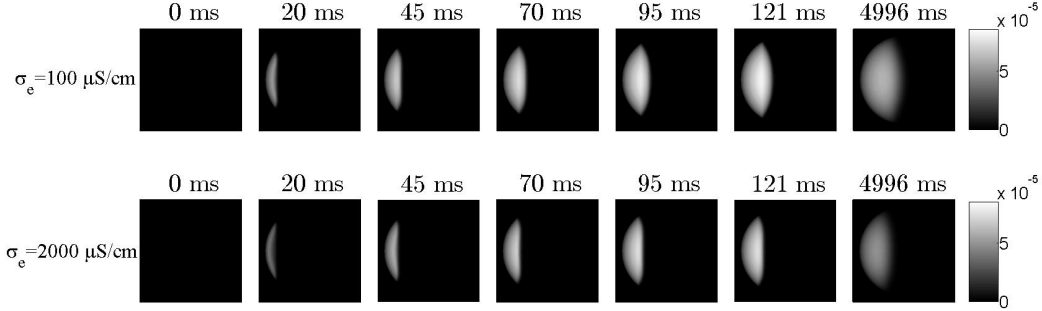


Figure 3: Contour plots of convoluted PIB concentration at the cell center-plane for  $\sigma_e = 100 \mu\text{S}/\text{cm}$  (top) and  $2000 \mu\text{S}/\text{cm}$  (bottom). The snapshots are taken at  $t = 0, 20, 45, 70, 95, 121$ , and  $4996$  ms, following the experimental presentation in Sadik13.

for the negative correlation between delivery and extra-cellular conductivity [1, 14, 44], and alternative mechanisms need to be identified.

Figure 3 shows exemplary simulated results in an attempt to reproduce the experimental fluorescence images in Sadik13 (Fig. 1 therein). The contour plot is based on the convoluted concentration of PIB:

$$[\text{PIB}]_{\text{conv}} = \int_{-\sigma_z/2}^{\sigma_z/2} [\text{PIB}] e^{-z^2/2\sigma_z^2} dz, \quad (10)$$

where  $\sigma_z$  is the focal depth of the microscopic system, and  $z$  is the axis perpendicular to image acquisition. This convolution is taken to approximate the effects of a finite focal depth in the experimental measurements [47]. The evolution with respect to the lowest ( $100 \mu\text{S}/\text{cm}$ ) and the highest ( $2000 \mu\text{S}/\text{cm}$ ) conductivities is shown, which is in qualitative agreement with data. Noticeably, the spread is stronger in case of  $\sigma_e = 100 \mu\text{S}/\text{cm}$ .

Figure 4 demonstrates the detailed evolution of the species concentrations, also for the two extreme values of  $\sigma_e$ . Figures 4a-d show  $[\text{PI}^{2+}]$  and  $[\text{B}]$  at different times along the cell centerline,  $x$ . Together, the results indicate that the binding sites are exhausted upon electrophoretic entry of the free ions in the presence of the 100-ms pulse. Continuous intra-cellular diffusion and association/dissociation occur after the pulse ceases. However, no appreciable molecular exchange across the membrane is predicted. Figures 4e and f show the  $[\text{PIB}]$  profile. This compound is responsible for the experimentally observed fluorescence emission, and the convoluted concentration as defined by Eq. (10) is assumed to be proportional to the fluorescence intensity. Dur-



ing the pulse, the front of [PIB] profile advances uniformly along the field direction due to binding-site exhaustion. The redistribution post-pulsation is due to intra-cellular redistribution of all species. In comparison with Fig. 3, the peaks observed therein are attributed to the convolution over a spherical cell geometry, which effect we have previously explained [47]. Finally, Figs. 4g and h show the sum of the free and bound ions. This quantity indicates the total PI concentration in the cell. For both values of  $\sigma_e$ , this summed concentration ( $\sim 10$  mM) is significantly higher than the extra-cellular PI concentration ( $100 \mu\text{M}$ ). Furthermore, consistent with the experimental observation, delivery decreases when  $\sigma_e$  increases. These trends are explained with an electrokinetic phenomenon termed Field-Amplified Sample Stacking (FASS), which is discussed in greater details in our previous work [47, 48].

To study total delivery, we integrate and sum the free and bound PI concentrations over the entire cell, and denote the resulting quantity by  $\text{PI}_{\text{tot}} + \text{PIB}_{\text{tot}}$ . The evolution of total delivery as a function of time and for the six values of  $\sigma_e$  is shown in Figs. 5a and b, where Fig. 5b displays the specific stage during the pulse. Once the pulse ceases, the total delivery,  $\text{PI}_{\text{tot}} + \text{PIB}_{\text{tot}}$ , does not further increase. This saturation of delivery is due to the fact that in the model, pores immediately return to a very small size ( $r_m = 0.8$  nm, [46]), hence significantly diminishing  $\rho_p$  and preventing post-pulsation diffusive delivery. A further examination on the effect of the latter is presented later in Fig. 6b. Figures 5c and d show the evolution of bound PI integrated over the whole cell ( $\text{PIB}_{\text{tot}}$ ). The results are in qualitative agreement with the total fluorescence intensity (TFI, induced by the compound PIB) presented in Sadik13. Figure 5c shows, in contrast to Fig. 5a, that  $\text{PIB}_{\text{tot}}$  continues to increase even after the pulse ceases. Although no more PI is delivered into the cell at this stage, the available free PI ions that have already entered the cell during the pulse (Figs. 4a and b) continue to spread and bind, causing  $\text{PIB}_{\text{tot}}$  to further increase. A final steady-state is reached within the diffusive time scale ( $\sim 0.1$  s) after the association/dissociation processes equilibrate over the entire cell.

Together, Figs. 4 and 5 impart important insights. First, due to the FASS mechanism and the high conductivity ratio, the cell can be “loaded” with a high concentration of ions via electrophoretic transport, even with short pulses. In the current simulations, this “loading” is sufficient to exhaust locally the high concentration of binding sites. A similar conclusion can be drawn if PI is replaced by other target agents such as drug molecules. Second, the observed increase in fluorescence signal post-pulsation, such as

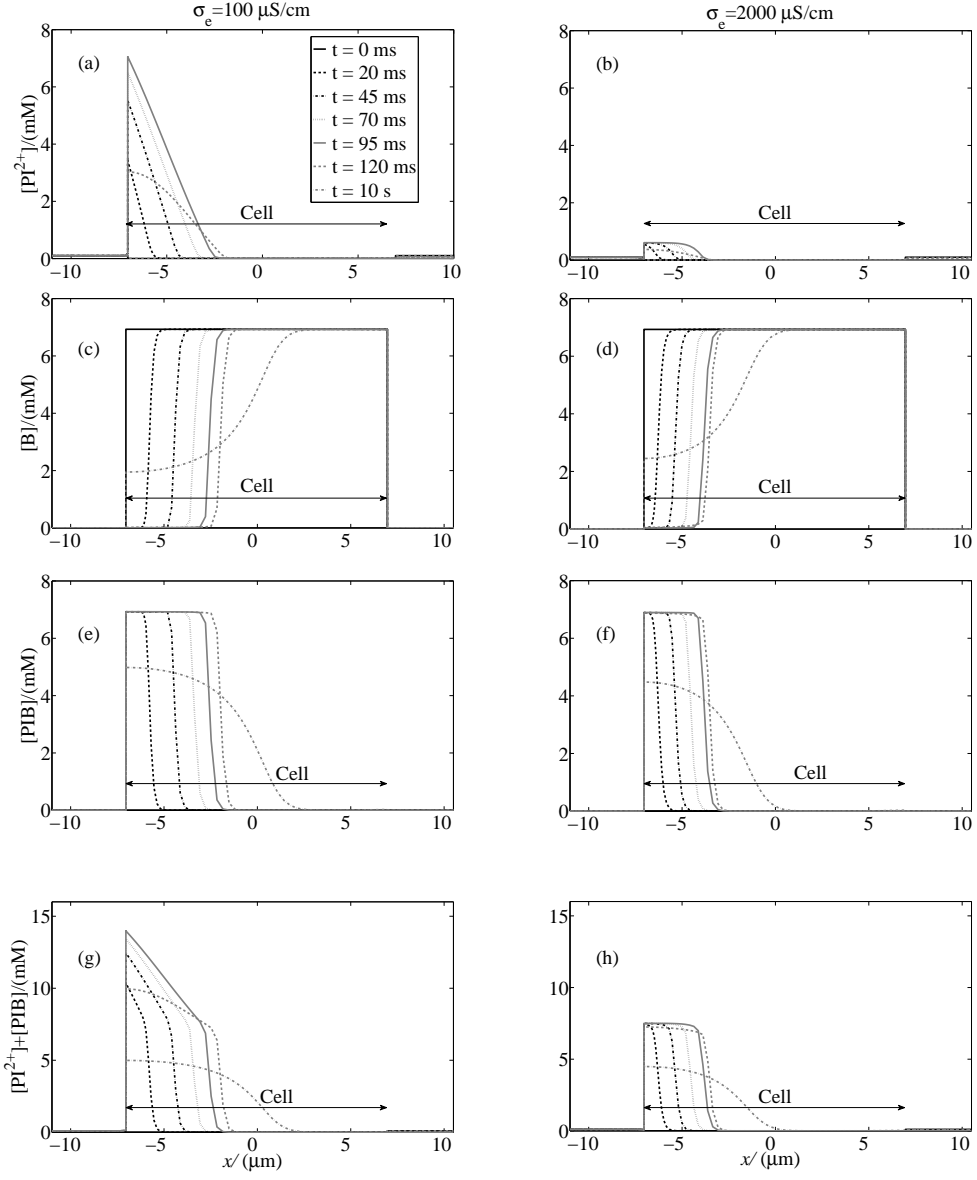


Figure 4: Species concentration evolution for  $\sigma_e = 100 \mu\text{S/cm}$  and  $2000 \mu\text{S/cm}$  along the cell centerline,  $x$ .

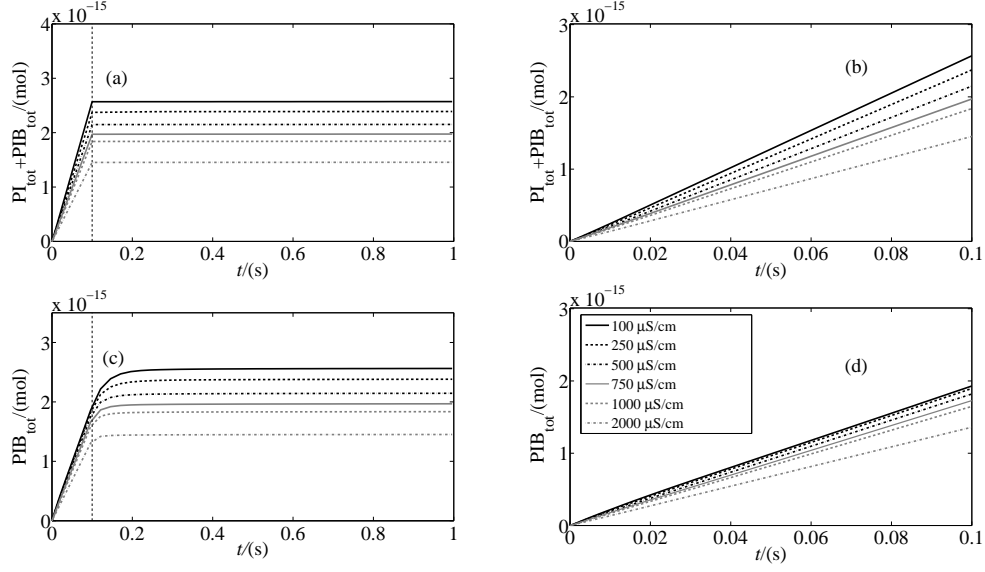


Figure 5: (a) Evolution of integrated free PI and PIB concentrations over the entire cell ( $PI_{tot} + PIB_{tot}$ ) for the six values of  $\sigma_e$ . The dashed vertical line indicates the end of the pulse. (b) Evolution of  $PI_{tot} + PIB_{tot}$  during the pulse. (c) Evolution of integrated PIB concentration over the entire cell ( $PIB_{tot}$ ). (d) Evolution of  $PIB_{tot}$  during the pulse.

that presented in Sadik13 may be partially attributed to this “pre-loading” effect. Therefore, caution needs to be taken to interpret experimental data where an indirect indicator such as PIB is used to study PI delivery.

Figure 6a compares the simulated results with data from Sadik13. The experimental data is denoted by circles, and the middle and lower curves represent contributions to the normalized TFI during and after the pulse, respectively. The upper curve is the sum of the two. The model prediction is denoted by pluses, and the definition of the curves follows the data. Because of the difference in the units of the measurement (a.u. for the fluorescence signal) and the prediction (mol for  $PIB_{tot}$ ), the axis presenting the latter is scaled linearly, such that the upper curves are best matched. The comparison demonstrates that the trends in the data are very-well captured by the numerical study, although we observe quantitative differences between the middle and lower curves. As noted above, in the model prediction, although  $PIB_{tot}$  continues to increase after the pulse, it is in actuality attributed to further binding of the free PI ions already delivered into the cell during the pulse.

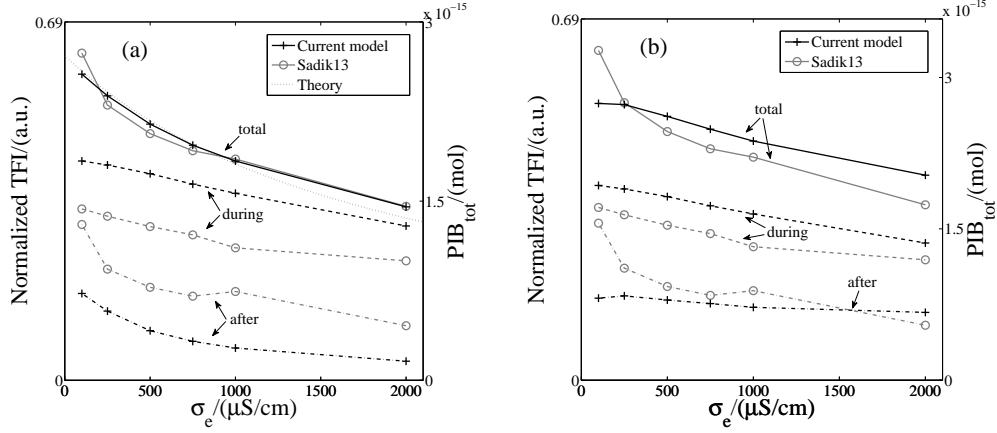


Figure 6: Comparison of simulated results ('+', right axis) with experimental data from Sadik13 ('o', left axis). For the data, the middle and lower curves represent contributions to the total fluorescence intensity (TFI) during and after the pulse, respectively. The upper curve is the sum of the two. In comparison, numerical simulation of  $\text{PIB}_{\text{tot}}$  is presented, and the upper, middle, and lower curves are defined similarly. The right axis is scaled linearly such that the upper curves from data and simulation best match. (a) Simulated results using the original ASE model. The solid line is a theoretical fitting with the functional form  $C/(2\sigma_e + \sigma_i)$ . (b) The size of the pores are artificially maintained for 1 s post-pulsation in the ASE model to allow for more diffusive delivery.

The correlation between  $\text{PIB}_{\text{tot}}$  and  $\sigma_e$  can be approximated by

$$\text{PIB}_{\text{tot}} \propto \frac{1}{2\sigma_e + \sigma_i}. \quad (11)$$

A fitting using this functional form is shown as the dotted line in Fig. 6a. This correlation can be derived if we assume that delivery is primarily mediated by electrophoresis. The molar flux into the cell is proportional to  $c_e E_e$ , where  $c_e$  is the extra-cellular concentration of  $\text{PI}^{2+}$ , and is assumed to be constant ( $[\text{PI}^{2+}]_{e,o}$ ). Therefore, molecular delivery is proportional to the extra-cellular field strength at the membrane. Using Eq. (2), the steady-state expression of  $E_e$  is given by

$$E_e = \frac{g_m V_m}{\sigma_e}. \quad (12)$$

Substituting Eq. (9) into Eq. (12), and considering  $V_m$  does not change with respect to the extra-cellular conductivity, we arrive at the correlation (11).

In the simulation above, and similar to our previous studies [47, 48],  $\rho_p$  decreases by three orders of magnitude immediately after the pulse ceases, due to the shrinking of the pore size in the absence of  $V_m$ . This reduction prohibits appreciable diffusive transport afterwards. This behavior is an artifact of the ASE model due to its incapability to include the resealing process (typically on the order of seconds to minutes [9, 19, 53]). To investigate the effects of post-pulsation diffusion, we artificially prevent  $\rho_p$  reduction at the end of the pulse. In other words, we keep  $\rho_p$  at its value at the end of the pulse for an additional second. The result is shown in Fig. 6b, also in comparison with the data. Similarly, the axis for  $\text{PIB}_{\text{tot}}$  is rescaled to best match the upper curves. We observe that the respective contributions from during and after the pulse match better quantitatively when comparing with Fig. 6a. However, the inverse trend with respect to  $\sigma_e$  is abated. This result is not surprising, as diffusive transport correlates positively with  $\rho_p$ , which in turn depends positively on  $\sigma_e$  (Fig. 2f). The addition of the diffusive delivery therefore weakens the inverse trend observed in the data.

In summary, the model prediction agrees qualitatively with the experimental data in general, and quantitatively in terms of the correlation between delivery and the extra-cellular conductivity (Eq. (11)). The results confirm that this inverse correlation is primarily mediated by electrophoretic transport during the pulse. In fact, this trend tends to be abated rather than enhanced by diffusive transport due to the positive dependence of permeabilization on extra-cellular conductivity. The current study suggests that electrophoretic transport may be important even for a small molecule such as PI.

#### 4. Conclusions

In this work, we have implemented a companion model study for the experimental counterpart by Sadik et al. [1]. Results on both membrane permeabilization and molecular delivery are presented, through which we gather useful insights on the system behavior.

The TMP in the permeabilized regions exhibits a consistent value across all six extra-cellular conductivities examined. Through a detailed investigation, we find that this value corresponds to a bifurcation point in the relation between equilibrium pore size and the TMP. This finding bears significance in that it connects the mesoscopic ASE model with macroscopic observables. In other words, this critical value was previously specified empirically in the

ASE model; with the current theory, it can be directly measured by fluorescence techniques following Kinoshita et al. [54] or Flickinger et al. [55].

Both the PAD and the membrane conductance are predicted to increase with an increasing extra-cellular conductivity. These correlations naturally result from the requirement to satisfy the Ohmic current conservation condition. In fact, the relation between membrane conductance and extra-cellular conductivity follows the functional form of  $g_m \propto \sigma_e / (2\sigma_e + \sigma_i)$ , which can be derived from an idealized model for the electric potential. This positive correlation between membrane permeabilization and extra-cellular conductivity rules out pure diffusive transport as a viable interpretation for the opposite effect of the latter on delivery.

For PI delivery, the model correctly predicts the inverse dependence on extra-cellular conductivity. This agreement confirms that this behavior is primarily mediated by electrophoretic transport during the pulse. In fact, diffusion tends to abate rather than enhance the trend. The correlation between delivery and extra-cellular conductivity is quantitatively captured by the model, namely,  $\text{PIB}_{\text{tot}} \propto 1 / (2\sigma_e + \sigma_i)$ . The simulation also reveals that an increase in the fluorescence intensity after the pulse ceases is not necessarily attributed to molecules entering the cell during this time; it may rise from continuous spreading and binding of free ions “loaded” into the cell in the presence of the pulse. Together, the results suggest that electrophoretic transport is important even for a small molecule such as PI.

Last but not least, a direct comparison between experimental data and model simulation as presented in this work helps establish confidence in and validate the latter. In the ASE model, a few parameters (such as  $\beta$ ,  $\gamma$ , and  $F_{\text{max}}$ , see Eq. (17) in Appendix B) are specified empirically following previous work. However, membrane permeabilization (including the PAD and membrane conductance) is found not to depend critically on the specific values of these parameters. Instead, the bifurcation point of the TMP, together with the Ohmic current conservation law strongly regulate the permeabilization behavior. The model therefore provides robust predictions which are useful for the study of electroporation-mediated molecular delivery.

## Acknowledgments

The authors acknowledge funding support from an NSF Award CBET-0747886 with Dr. Henning Winter and Dr. Dimitrios Papavassiliou as contract monitors.

## Appendix A: Mathematical definition of pertinent variables

### *Transmembrane Potential (TMP)*

The transmembrane potential,  $V_m$ , at any membrane location,  $\theta$ , is defined by the potential jump across the membrane:

$$V_m(t, \theta) = [\Phi_i(t, \theta) - \Phi_e(t, \theta)]|_{r=a} . \quad (13)$$

### *Total ionic current density*

The total ionic current density  $j_p$  is the summed electric current density over all electropores on a local element, defined by:

$$j_p(t, \theta) = \sum_{j=1}^{K(t, \theta)} i_p(r_j(t, \theta), V_m) / \Delta A, \quad (14)$$

where  $\Delta A$  is the area of the local element,  $K$  is the total number of conductive pores, and  $i_p$  denotes the current through an individual pore with radius  $r_j$  and subject to a transmembrane potential  $V_m$ .  $i_p$  is given by the formula:

$$i_p = \frac{2\pi r_j^2 \sigma_{eff} V_m}{\pi r_j + 2h}, \quad (15)$$

where  $\sigma_{eff} = (\sigma_e - \sigma_i) / \ln(\sigma_e / \sigma_i)$  is an effective pore conductivity, and  $h$  is the membrane thickness. A detailed derivation of Eq. (15) can be found in our previous work [24].

### *Pore area density (PAD)*

The pore area density  $\rho_p$  is the fractional area occupied by the conductive pores at a specific point on the membrane, defined by the following formula:

$$\rho_p(t, \theta) = \sum_{j=1}^{K(t, \theta)} \pi r_j^2 / \Delta A, \quad (16)$$

where the definition of  $\Delta A$ ,  $K$  and  $r_j$  are the same as in Eq. (14).  $\rho_p$  is used as a measurement of the membrane permeabilization level.

## Appendix B: The equilibrium transmembrane potential

In Figs. 2a and b, we find that the TMP,  $V_m$ , settles to an equilibrium value in the permeabilized regions within a few microseconds after the pulse starts. Furthermore, this value does not vary appreciably with respect to the extra-cellular conductivity. Here we argue that this value is determined by a critical point in the pitchfork bifurcation in the  $(r_{eq}, V_m)$  relation, where  $r_{eq}$  is the equilibrium pore size at a given voltage.

In the ASE we use, and in general in the Smoluchowski equations governing the pore dynamics [20, 46, 56], the pore size evolves to minimize membrane energy. The rate of change is given by the equation [46]:

$$\dot{r} = \frac{D_p}{K_B T} \left[ \frac{4r_p^4 \beta}{r^5} - 2\pi\gamma + 2\pi\sigma_{eff}r + \frac{F_{max}V_m^2}{1 + \frac{r_h}{r+r_t}} \right], \quad (17)$$

where  $r$  is the pore radius,  $D_p$  is the pore radius diffusion coefficient,  $K_B$  is the Boltzmann constant, and  $T$  is temperature. The value of  $\sigma_{eff}$  is given by  $\sigma_{eff} = 2\sigma' - \frac{2\sigma' - \sigma_0}{(1 - \rho_p)^2}$ .  $\beta$ ,  $\gamma$ ,  $F_{max}$ ,  $r_h$ ,  $r_c$ ,  $\sigma'$ , and  $\sigma_0$  are model constants, and the values can be found in [46]. This equation can be written in a generalized form as:

$$\dot{r} = U(r, V_m, \rho_p). \quad (18)$$

The equilibrium value for the pore size,  $r_{eq}$ , can be found by setting the right hand side of Eq. (18) to zero:

$$U(r_{eq}, V_m, \rho_p) = 0. \quad (19)$$

In general, the dependence of  $r_{eq}$  on  $\rho_p$  is weak. On the other hand, its dependence on  $V_m$  exhibits an interesting pitchfork bifurcation, which is shown in Fig. 7a, for an exemplary value of  $\rho_p = 2 \times 10^{-3}$ .

The coupled dynamics between  $r_{eq}$  and  $V_m$  in the initial charging and permeabilization processes are illustrated in Figs. 7a and b, where the four stages are denoted by I-IV. In Stage I, the initial charging stage, the membrane is near-impermeable with sub-nanometer pores, and  $V_m$  grows rapidly via capacitive charging (see Eq. (2)). Once  $V_m$  reaches  $V_m^{crit}$ , the bifurcation point, pores begin to expand significantly. Due to the consequent “jump” in  $g_m$  (Stage II),  $V_m$  eventually has to decrease to satisfy the current continuity condition (Stage III), until the upper branch of the bifurcation is reached.  $V_m$  continues to decrease until it reaches the other critical point,  $V_m^{eq}$ , where the



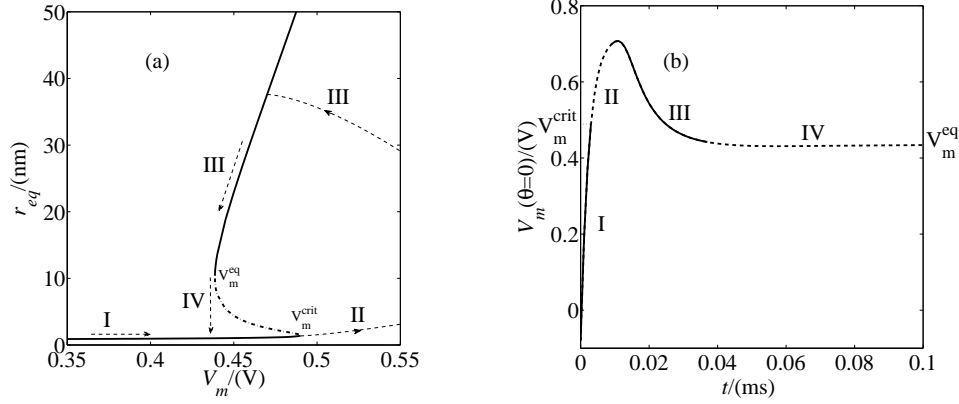


Figure 7: Schematics for the  $(r_{eq}, V_m)$  dynamics. (a) The relation between  $r_{eq}$  and  $V_m$  exhibits a pitchfork bifurcation behavior. Between  $V_m^{eq}$  and  $V_m^{crit}$ , three branches of solutions exist from Eq. (19), where the middle one (dash-dotted) is unstable. The initial charging and permeabilization process follows four stages denoted by I-IV. For this case  $\rho_p = 2 \times 10^{-3}$ . A detailed description is given in the text. (b) Exemplary evolution of  $V_m$  as a function of time. The stages I-IV correspond to those in (a).

pore size begins to recover to the lower branch (Stage IV). The dependence of pore radius on  $V_m$  exhibits hysteresis typical of this type of bifurcation. The point around  $V_m^{eq}$  is the most interesting, because two equilibrium pore sizes exist. For this reason,  $g_m$  can assume a range of values for a single value of  $V_m$ . The upper bound can be calculated by assuming all pores are on the upper branch,  $r_{eq} = 10.4$  nm; the lower bound, the lower branch,  $r_{eq} = 1.01$  nm. If the required steady-state value of  $g_m$  to satisfy the current density continuity condition (Eq. (2)) lies within these two bounds, then  $V_m$  maintains at the level of  $V_m^{eq}$ . This phenomenon is analogous to phase change in physics, where  $V_m^{eq}$  assumes the role of, e.g., temperature. For the same argument,  $V_m^{crit}$  is another candidate for the equilibrium value of  $V_m$ , which in general occurs when less number of pores are locally available, e.g., at the edges of the permeabilized regions. (See the slightly increased  $V_m$  values near  $\theta = \pi/4$ ,  $3\pi/4$  in Fig. 2b.) Although the above illustration is only schematic, the full-model simulation follows this general pattern.

We remark that this finding bears significance in that it connects the mesoscopic ASE model with macroscopic observables. The membrane energy model in the ASE, based on which Eq. (17) is derived, has a few free constants. In general, these constants cannot be directly measured. The

above analysis reveals that if pores on the membrane do follow the bifurcation behavior with respect to the TMP, then the critical values, namely,  $V_m^{eq}$  and  $V_m^{crit}$  can be directly observed via a fluorescence measurement similar to that by Kinosita et al. [54] or Flickinger et al. [55]. These values can in turn help determine the pertinent constants (such as  $\beta$ ,  $\gamma$ , and  $F_{max}$ ) used in the model.

## References

- [1] M. M. Sadik, J. Li, J. W. Shan, D. I. Shreiber, H. Lin, Quantification of propidium iodide delivery using milisecond electric pulses: Experiments, *BBA Biomembranes* 1828 (2013) 1322–1328.
- [2] E. Neumann, M. Schaefer-Ridder, Y. Wang, P. H. Hofschneider, Gene transfer into mouse lyoma cells by electroporation in high electric fields, *The EMBO Journal* 1 (1982) 841–845.
- [3] L. M. Mir, Therapeutic perspectives of in vivo cell electroporomeabilization, *Bioelectrochemistry* 53 (2000) 1–10.
- [4] J. Gehl, Electroporation: theory and methods, perspectives for drug delivery, gene therapy and research, *Acta Physiol. Scand.* 177 (2003) 437–447.
- [5] F. André, L. M. Mir, DNA electrotransfer: its principles and an updated review of its therapeutic applications, *Gene Ther.* 11 (2004) S33–S42.
- [6] K. H. Schoenbach, R. P. Joshi, J. F. Kolb, N. Chen, M. Stacey, P. F. Blackmore, E. S. Buescher, S. J. Beebe, Ultrashort electrical pulses open a new gateway into biological cells, *Proc. IEEE* 92 (2004) 1122–1136.
- [7] A. Van Driessche, P. Ponsaerts, D. R. Van Bockstaele, V. F. I. Van Tendeloo, Z. N. Bernema, Messenger RNA electroporation: an efficient tool in immunotherapy and stem cell research, *Folia Histochemica et Cytobiologica* 43 (2005) 213–216.
- [8] M. Costa, M. Dottori, K. Sourris, P. Jamshidi, T. Hatzistavrou, R. Davis, L. Azzola, S. Jackson, S. M. Lim, M. Pera, A. G. Elefanty, E. G. Stanley, A method for genetic modification of human embryonic stem cells using electroporation, *Nat. Protoc.* 2 (2007) 792–796.

- [9] J.-M. Escoffre, T. Portet, L. Wasungu, J. Teissié, D. Dean, M.-P. Rols, What is (still not) known of the mechanism by which electroporation mediates gene transfer and expression in cells and tissues, *Mol Biotechnol* 41 (2009) 286–295.
- [10] J. Teissié, J.-M. Escoffre, A. Paganin, S. Chabot, E. Bellard, L. Wasungu, M.-P. Rols, M. Golzio, Drug delivery by electropulsation: Recent developments in oncology, *Int. J. Pharm.* 423 (2012) 3–6.
- [11] D. C. Chang, T. S. Reese, Changes in membrane structure induced by electroporation as revealed by rapid-freezing electron microscopy, *Biophys. J.* 58 (1990) 1–12.
- [12] C. Wilhelm, M. Winterhalter, U. Zimmermann, R. Benz, Kinetics of pore size during irreversible electrical breakdown of lipid bilayer membranes, *Biophys. J.* 64 (1993) 121–128.
- [13] M. Spassova, I. Tsoneva, A. G. Petrov, J. I. Petkova, E. Neumann, Dip patch clamp currents suggest electrodiffusive transport of the polyelectrolyte dna through lipid bilayers, *Biophys. Chem.* 52 (1994) 267–274.
- [14] C. S. Djuzenova, U. Zimmermann, H. Frank, V. L. Sukhorukov, E. Richter, G. Fuhr, Effect of medium conductivity and composition on the uptake of propidium iodide into electropermeabilized myeloma cells, *Biochim. Biophys. Acta* 1284 (1996) 143–152.
- [15] L. H. Wegner, B. Flickinger, C. Eing, T. Berghöfer, P. Hohenberger, W. Frey, P. Nick, A patch clamp study on the electro-permeabilization of higher plant cells: Supra-physiological voltages induce a high-conductance, K<sup>+</sup> selective state of the plasma membrane, *Biochim. Biophys. Acta* 1808 (2011) 1728–1736.
- [16] T. B. Napotnik, Y.-H. Wu, M. A. Gundersen, D. Miklavčič, P. T. Vernier, Nanosecond electric pulses cause mitochondrial membrane permeabilization in jurkat cells, *Bioelectromagnetics* 33 (2012) 257–264.
- [17] P. Kramar, L. Delemotte, A. M. Lebar, M. Kotulska, M. Tarek, D. Miklavčič, Molecular-level characterization of lipid membrane electroporation using linearly rising current, *Journal of Membrane Biology* 245 (2012) 651–659.

- [18] A. Barnett, J. C. Weaver, Electroporation: a unified, quantitative theory of reversible electrical breakdown and mechanical rupture in artificial planar bilayer membranes, *Bioelectrochem. Bioenerg.* 25 (1991) 163–182.
- [19] J. C. Weaver, Y. A. Chizmadzhev, Theory of electroporation: A review, *Bioelectrochem. Bioenerg.* 41 (1996) 135–160.
- [20] J. C. Neu, W. Krassowska, Asymptotic model of electroporation, *Phys. Rev. E* 59 (1999) 3471–3482.
- [21] H. Leontiadou, A. E. Mark, S. J. Marrink, Molecular dynamics simulations of hydrophilic pores in lipid bilayers, *Biophys. J.* 86 (2004) 2156–2164.
- [22] M. Tarek, Membrane electroporation: A molecular dynamics simulation, *Biophys. J.* 88 (2005) 4045–4053.
- [23] Z. A. Levine, P. T. Vernier, Life cycle of an electropore: Field-dependent and field-independent steps in pore creation and annihilation, *J Membrane Biol* 236 (2010) 27–36.
- [24] J. Li, H. Lin, The current-voltage relation for electropores with conductivity gradients, *Biomicrofluidics* 4 (2010) 013206.
- [25] S. I. Sukharev, V. A. Klenchin, S. M. Serov, L. V. Chernomordik, Y. A. Chizmadzhev, Electroporation and electrophoretic DNA transfer into cells: the effect of DNA interaction with electropores, *Biophys. J.* 63 (1992) 1320–1327.
- [26] M. R. Prausnitz, J. D. Corbett, J. A. Gimm, D. E. Golan, R. Langer, J. C. Weaver, Millisecond measurement of transport during and after an electroporation pulse, *Biophys. J.* 68 (1995) 1864–1870.
- [27] L. M. Mir, M. F. Bureau, J. Gehl, R. Rangara, D. Rouyi, J.-M. Caillaud, P. Delaere, D. Branelleci, B. Schwartz, D. Scherman, High-efficiency gene transfer into skeletal muscle mediated by electric pulses, *Proc. Natl. Acad. Sci.* 96 (1999) 4262–4267.
- [28] M.-P. Rols, J. Teissié, Electroporabilization of mammalian cells to macromolecules: Control by pulse duration, *Biophys. J.* 75 (1998) 1415–1423.

- [29] C. Faurie, E. Phez, M. Golzio, C. Vossen, J.-C. Lesbordes, C. Delteil, J. Teissié, M.-P. Rols, Effect of electric field vectoriality on electrically mediated gene delivery in mammalian cells, *Biochim. Biophys. Acta* 1665 (2004) 92–100.
- [30] S. Šatkauskas, M. F. Bureau, M. Puc, A. Mahfoudi, D. Scherman, D. Miklavčič, L. M. Mir, Mechanisms of in vivo DNA electrotransfer: Respective contributions of cell electropermeabilization and DNA electrophoresis, *Molecular Therapy* 5 (2002) 133–140.
- [31] S. Šatkauskas, F. André, M. F. Bureau, D. Scherman, D. Miklavčič, L. M. Mir, Electrophoretic component of electric pulses determines the efficacy of in vivo DNA electrotransfer, *Hum. Gene Ther.* 16 (2005) 1194–1201.
- [32] N. Pavšelj, V. Préat, DNA electrotransfer into the skin using a combination of one high- and one low-voltage pulse, *J. Controlled Release* 106 (2005) 407–415.
- [33] F. Liu, S. Heston, L. M. Shollenberger, B. Sun, M. Mickle, M. Lovell, L. Huang, Mechanism of in vivo DNA transport into cells by electroporation: electrophoresis across the plasma membrane may not be involved, *Journal of Gene Medicine* 8 (2006) 353–361.
- [34] G. Pucihar, T. Kotnik, D. Miklavčič, J. Teissié, Kinetics of transmembrane transport of small molecules into electropermeabilized cells, *Biophys. J.* 95 (2008) 2837–2848.
- [35] M. Kandušer, D. Miklavčič, M. Pavlin, Mechanisms involved in gene electrotransfer using high- and low-voltage pulses - an in vitro study, *Bioelectrochemistry* 74 (2009) 265–271.
- [36] D. Miklavčič, L. Towhidi, Numerical study of the electroporation pulse shape effect on molecular uptake of biological cells, *Radiol Oncol* 44 (2010) 34–41.
- [37] M. Pavlin, K. Flisar, M. Kandušer, The role of electrophoresis in gene electrotransfer, *J. Membrane Biol.* 236 (2010) 75–79.

- [38] K. C. Smith, J. C. Weaver, Transmembrane molecular transport during versus after extremely large, nanosecond electric pulses, *Biochem. Biophys. Res. Commun.* 412 (2011) 8–12.
- [39] J. L. Vázquez, J. Gehl, G. G. Hermann, Electroporation enhances mitomycin C cytotoxicity on T24 bladder cancer cell line: A potential improvement of intravesical chemotherapy in bladder cancer, *Bioelectrochemistry* 88 (2012) 127–133.
- [40] U. Zimmermann, R. Schnettler, G. Klöck, H. Watzka, Mechanisms of electrostimulated uptake of macromolecules into living cells, *Naturwissenschaften* 77 (1990) 543–545.
- [41] M. Wu, F. Yuan, Membrane binding of plasmid DNA and endocytic pathways are involved in electrotransfection of mammalian cells, *PLoS ONE* 6 (2011) e20923.
- [42] R. Lin, D. C. Chang, Y.-K. Lee, Single-cell electroendocytosis on a micro chip using in situ fluorescence microscopy, *Biomed. Microdevices* 13 (2011) 1063–1073.
- [43] C. Rosazza, E. Phez, J.-M. Escoffre, L. Cézanne, A. Zumbusch, M.-P. Rols, Cholesterol implications in plasmid DNA electrotransfer: Evidence for the involvement of endocytotic pathways, *Int. J. Pharm.* 423 (2012) 134–143.
- [44] K. J. Müller, V. L. Sukhorukov, U. Zimmermann, Reversible electroporomeabilization of mammalian cells by high-intensity, ultra-short pulses of submicrosecond duration, *J. Membrane Biol.* 184 (2001) 161–170.
- [45] J. C. Neu, W. Krassowska, Modeling postshock evolution of large electropores, *Phys. Rev. E* 67 (2003) 021915.
- [46] W. Krassowska, P. D. Filev, Modeling electroporation in a single cell, *Biophys. J.* 92 (2007) 404–417.
- [47] J. Li, H. Lin, Numerical simulation of molecular uptake via electroporation, *Bioelectrochemistry* 82 (2011) 10–21.
- [48] J. Li, W. Tan, M. Yu, H. Lin, The effect of extracellular conductivity on electroporation mediated molecular delivery, *BBA Biomembranes* 1828 (2012) 461–470.

- [49] M. M. Sadik, M. Yu, J. W. Shan, D. I. Shreiber, H. Lin, Scaling relationship and optimization of double-pulse electroporation, *Biophys. J.*, accepted (2013).
- [50] P. M. Vlahovska, R. S. Gracià, S. Aranda-Espinoza, R. Dimova, Electrohydrodynamic model of vesicle deformation in alternating electric fields, *Biophys. J.* 96 (2009) 4789–4803.
- [51] M. M. Sadik, J. Li, J. W. Shan, D. I. Shreiber, H. Lin, Vesicle deformation and poration under strong dc electric fields, *Phy. Rev. E.* 83 (2011) 066316.
- [52] D. O. H. Suzuki, A. Ramos, M. C. M. Ribeiro, L. H. Cazarolli, F. R. M. B. Silva, L. D. Leite, J. L. B. Marques, Theoretical and experimental analysis of electroporated membrane conductance in cell suspension, *IEEE Trans. Biomed. Eng.* 58 (2011) 3310–3318.
- [53] H. He, D. C. Chang, Y.-K. Lee, Nonlinear current response of micro electroporation and resealing dynamics for human cancer cells, *Bioelectrochemistry* 72 (2008) 161–168.
- [54] K. Kinosita Jr., I. Ashikawa, N. Saita, H. Yoshimura, H. Itoh, K. Nagayama, A. Ikegami, Electroporation of cell membrane visualized under a pulsed-laser fluorescence microscope, *Biophys. J.* 53 (1988) 1015–1019.
- [55] B. Flickinger, T. Berghöfer, P. Hohenberger, C. Eing, W. Frey, Transmembrane potential measurements on plant cells using the voltage-sensitive dye ANNINE-6, *Protoplasma* 247 (2010) 3–12.
- [56] S. A. Freeman, M. A. Wang, J. C. Weaver, Theory of electroporation of planar bilayer membranes: Predictions of the aqueous area, change in capacitance, and pore-pore separation, *Biophys. J.* 67 (1994) 42–56.